Spectroscopic and Computational Insights into Second-Sphere Amino-Acid Tuning of Substrate Analogue/Active-Site Interactions in Iron(III) Superoxide Dismutase

Laurie E. Grove[†], **Juan Xie**[†], **Emine Yikilmaz**[§,⊥], **Anush Karapetyan**[§,‡], **Anne-Frances Miller**[§], and **Thomas C. Brunold**[*,†]

[†]University of Wisconsin-Madison

[§]University of Kentucky

[⊥]Current Address: Berlex Biosciences, 2600 Hilltop Dr., Richmond CA, 94806.

[‡]Current Address: Pathology & Laboratory Medicine, Medical Center, University of Kentucky

Abstract

In this study the mechanism by which second-sphere residues modulate the structural and electronic properties of substrate-analogue complexes of the Fe-dependent superoxide dismutase (FeSOD) has been explored. Both spectroscopic and computational methods were used to investigate the azide (N_3^-) adducts of Fe^{3+}SOD (N_3-Fe^{3+}SOD) and its Q69E mutant, as well as Fe^{3+}-substituted MnSOD (N_3-Fe^{3+}(Mn)SOD) and its Y34F mutant. Electronic absorption, circular dichroism, and magnetic circular dichroism spectroscopic data reveal that the energy of the dominant $N_3^- \rightarrow Fe^{3+}$ ligand-to-metal charge transfer (LMCT) transition decreases in the order N_3-Fe^{3+}(Mn)SOD > N_3-Fe^{3+}SOD > Q69E N_3-Fe^{3+}SOD. Intriguingly, the LMCT transition energies correlate almost linearly with the $Fe^{3+/2+}$ reduction midpoint potentials of the corresponding Fe^{3+}-bound SOD species in the absence of azide, which span a range of ~1 V (see preceding paper). To explore the origin of this correlation, combined quantum mechanics/molecular mechanics (QM/MM) geometry optimizations were performed on complete enzyme models. The INDO/S-CI computed electronic transition energies satisfactorily reproduce the experimental trend in LMCT transition energies, indicating that the QM/MM optimized active-site models are reasonable. Density functional theory calculations on these experimentally validated active-site models reveal that the differences in spectral and electronic properties among the four N_3^- adducts arise primarily from differences in the hydrogen-bond network involving the conserved second-sphere Gln (mutated to Glu in Q69E FeSOD) and the solvent ligand. The implications of our findings with respect to the mechanism by which the second-coordination

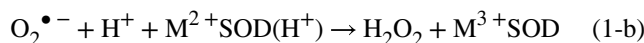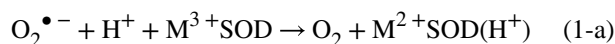sphere modulates substrate-analogue binding as well as the catalytic properties of FeSOD are discussed.

Graphical Abstract:

Spectroscopic and computational methods were used to study the azide (a substrate analogue) complexes of Fe^{3+} superoxide dismutase ($Fe^{3+}SOD$), Fe^{3+}-substituted Mn superoxide dismutase ($Fe^{3+}(Mn)SOD$), Q69E $Fe^{3+}SOD$, and Y34F $Fe^{3+}(Mn)SOD$. While all species form a similar azide-Fe^{3+} adduct, the energy of the dominant azide-to-Fe^{3+} charge transfer transition varies considerably, correlating almost quantitatively with the corresponding $Fe^{3+/2+}$ reduction potentials of the azide-free forms. Our results reveal that these spectral differences arise primarily from different hydrogen-bonding interactions between second-sphere residues and the Fe^{3+}-bound solvent ligand.
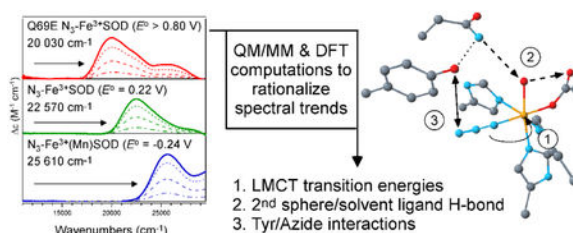
1.   Introduction

Superoxide dismutases (SODs) are metalloenzymes whose function is to protect biological systems from oxidative damage stemming from the superoxide radical anion ($O_2^{\bullet-}$) that is generated by incomplete reduction of O_2.[1, 2] In the four known types of SODs, the active site contains either Fe, Mn, Ni, or Cu and Zn. The Fe-dependent SODs (FeSODs) are mostly found in prokaryotes, whereas the highly homologous Mn-dependent SODs (MnSODs) are present in both eukaryotes and prokaryotes. The Cu/ZnSOD and NiSOD, which are found in eukaryotes and some bacterial *Streptomyces* species, respectively, are structurally unrelated to each other as well as the Fe- and MnSODs.[3–5] Like all SODs, the Fe- and Mn-dependent enzymes disproportionate $O_2^{\bullet-}$ into molecular oxygen and hydrogen peroxide using a ping-pong mechanism. In this proton-coupled electron-transfer process, the metal ion cycles between the +3 and +2 oxidation states (eq 1, where the metal ion M is either Fe or Mn).[6, 7] To ensure rapid turnover, the reduction potential, E^o, of the enzyme must lie approximately halfway between the potentials associated with the conversion of $O_2^{\bullet-}$ to O_2 and H_2O_2 (−330 mV and +890 mV vs. NHE at pH 7, respectively).[8]

$$O_2^{\bullet-} + H^+ + M^{3+}SOD \rightarrow O_2 + M^{2+}SOD(H^+) \quad (1\text{-}a)$$

$$O_2^{\bullet-} + H^+ + M^{2+}SOD(H^+) \rightarrow H_2O_2 + M^{3+}SOD \quad (1\text{-}b)$$

FeSOD and MnSOD from *Eschericia coli* are closely related proteins with very similar amino-acid sequences and virtually identical active-site structures (Figure 1).[9–17] In the resting state of each protein, the metal ion is in a trigonal bipyramidal coordination environment consisting of two His residues and an Asp residue in the equatorial plane, and a His residue and a solvent molecule (believed to be OH^- and H_2O in the M^{3+} and M^{2+} states, respectively) in the axial positions.[15, 18] Despite their structural similarities, FeSOD and MnSOD display distinct metal specificities; that is, neither Fe-substituted MnSOD (Fe(Mn)SOD), nor Mn-substituted FeSOD (Mn(Fe)SOD) show significant catalytic activity at neutral pH.[19–23] A straightforward explanation for this puzzling result was provided by Vance and Miller, who demonstrated that the $M^{3+/2+}$ reduction potentials of the metal-substituted SODs are drastically altered from those of the native enzymes.[24] Specifically, the $E°$ of ~ –240 mV (vs. NHE) measured for Fe(Mn)SOD is depressed too much from FeSOD's $E°$ of ~20–220 mV to support substrate oxidation activity (eq 1-a).[24] Conversely, the $E°$ of >690 mV determined for Mn(Fe)SOD is sufficiently elevated from MnSOD's $E°$ of 290 mV to preclude $O_2^{•-}$ reduction (eq 1-b).[25]

The most striking structural difference between the FeSOD and MnSOD active sites is the different positioning of the second-sphere Gln, which corresponds to residue 69 in FeSOD and residue 146 in MnSOD (Figure 1). Gln69/146 is central to a hydrogen-bond network that also includes the metal-bound solvent molecule and Tyr34 (Figure 1, dashed lines).[15, 26, 27] However the hydrogen bond between the Gln69/146 side chain and the coordinated solvent is much stronger in MnSOD than in FeSOD, which may explain the vastly different reduction potentials of the native and metal-substituted enzymes.[24, 28] In support of this hypothesis, the Q69E FeSOD mutant, in which the hydrogen-bond donor Gln69 is replaced by a potential hydrogen-bond acceptor, has an $E°$ of >600 mV and thus displays less than 1% of wild-type (WT) FeSOD activity.[29–31] A quantitative exploration of the molecular basis for the different metal ion reduction potentials of WT FeSOD, Fe(Mn)SOD, and Q69E FeSOD is presented in the preceding paper.[32]

To obtain molecular-level insight into the reaction mechanisms employed by Fe- and MnSODs, it would be desirable to study the nature of the substrate/active-site interactions. However, the rate of $O_2^{•-}$ dismutation by SODs approaches the diffusion-controlled limit, making it virtually impossible to trap any intermediates. Therefore, azide (N_3^-), a competitive inhibitor of SODs that possesses similar frontier orbitals and the same charge as $O_2^{•-}$, has been repeatedly used as a substrate analogue in mechanistic studies of SODs.[7, 15, 27, 33–40] X-ray crystallographic data have revealed that in both Fe^{3+}- and Mn^{3+}SODs, azide binds between the two equatorial His residues to form a distorted octahedral complex.[15, 41] However, the orientation of the N_3^- ligand in the corresponding azide adducts is strikingly different (Figure 2), despite the fact that the first coordination spheres of the resting enzymes are virtually identical (Figure 1). In N_3-Mn^{3+}SOD from *T. thermophilus*, azide forms a hydrogen bond with Tyr34, whereas in N_3-Fe^{3+}SOD, it points away from Tyr34 and into the substrate access channel. Since oxidation of the superoxide anion by the M^{3+}SODs is believed to follow an inner-sphere mechanism, the different substrate analogue binding modes suggest that the actual substrate could also bind differently and experience different reaction barriers for electron transfer.

In this study, we have characterized the azide-adducts of Fe^{3+}SOD, Fe^{3+}(Mn)SOD, and Q69E Fe^{3+}SOD using electronic absorption (Abs), circular dichroism (CD) and magnetic circular dichroism (MCD) spectroscopies to explore how changes in the Gln69/146···O(Sol) hydrogen bond influence the geometric and electronic properties of the active-site azide– Fe^{3+} complex. Furthermore, to evaluate the possibility that Tyr34 interacts with the azide ligand in N_3-Fe^3(Mn)SOD, we have also prepared and characterized the azide adduct of the Tyr34 → Phe mutant of Fe(Mn)SOD. As no X-ray crystal structures are available for the N_3^- complexes of Fe^{3+}(Mn)SOD, Y34F Fe^{3+}(Mn)SOD, and Q69E Fe^{3+}SOD, complete enzyme models for these species were generated by carrying out combined quantum mechanics/molecular mechanics (QM/MM) geometry optimizations. The corresponding active-site models were validated on the basis of our spectroscopic data by using semi-empirical INDO/S-CI and density functional theory (DFT) computations. The results obtained in this combined spectroscopic/computational study provide significant new insight into the mechanism by which second-sphere amino-acids modulate the substrate analogue/ active-site interactions in Fe^{3+}SOD.

2. Experimental Section

2.1. Protein Samples.

WT FeSOD, Fe(Mn)SOD, and Q69E FeSOD were prepared according to published procedures,[33,37] as outlined in the preceding paper.[32] The gene for Y34F MnSOD was constructed by polymerase chain reaction using the megaprimer method.[43] Both strands of the mutant gene were sequenced to confirm the presence of the desired mutation and to ascertain that no additional mutations had occurred. Y34F Fe(Mn)SOD was produced by in-vivo metal ion substitution wherein the over-expressing strain was cultured in minimal medium lacking Mn and supplemented with Fe, at low aeration. The resulting Y34F Fe(Mn)SOD contained predominantly Fe (>90%) and displayed 10% WT FeSOD activity at neutral pH, consistent with previous reports that Y34F Fe(Mn)SOD possesses low but significant activity.[42] Protein and azide concentrations used in our experiments are given in the figure captions.

2.2. Spectroscopy.

Variable-temperature Abs, CD, and MCD spectra were recorded using a Jasco J-715 spectropolarimeter in conjunction with a superconducting magnetocryostat (Oxford Instruments SM-4000 8T). To eliminate contributions from the natural CD to the MCD signal, the difference was taken between data obtained with the magnetic field aligned parallel and anti-parallel to the light propagation axis. Variable-temperature variable-field (VTVH) MCD data were obtained by measuring the signal intensity as a function of applied magnetic field at 2, 4, 8, and 15 K. VTVH MCD data were analyzed using the software developed by Dr. Frank Neese (University of Bonn, Germany).[46] All samples were in 50 mM potassium phosphate buffer (pH 7.0) with 55% (v/v) glycerol to ensure glass formation upon freezing.

2.3. Computations:

2.3.1. QM/MM geometry optimizations.—Input files for QM/MM geometry optimizations of entire protein subunits were generated from suitably chosen X-ray crystallographic coordinate files using the pdb2adf program developed by M. Swart (2002). For each model, the QM region included the metal ion, all first-sphere residues (including the coordinated solvent and exogenous azide ligand), along with Tyr34, Trp122 (Trp128 for Fe(Mn)SOD) and Gln69 (Glu69 and Gln146 for Q69E FeSOD and Fe(Mn)SOD, respectively). The MM region included all other atoms as well as the amide moieties of the amino acids that were treated at the QM level. The input coordinates for our N_3-Fe^{3+}SOD model were based on the corresponding X-ray crystallographic structure (PDB file 1ISC), using the subunit containing the 6-coordinate, azide-bound Fe^{3+} center.[15] As no X-ray structural data are available for the other three species included in this study, the starting models for QM/MM geometry optimizations were generated as follows. In the case of N_3-Fe^{3+}(Mn)SOD, the structure of Fe(Mn)SOD (PDB file 1MMM)[47] was used except that the exogenous OH^- ligand occupying the sixth coordination site of the Fe center in one subunit was replaced by N_3^-. This initial structural model was also used for Y34F N_3-Fe^{3+}(Mn)SOD, with the modification that the phenol functionality of Tyr34 was replaced with an H atom. For both the N_3-Fe^{3+}(Mn)SOD and Y34F N_3-Fe^{3+}(Mn)SOD species, two input models were generated: one in which the azide ligand hydrogen bonds to residue 34 as in N_3-Mn^{3+}SOD and the other in which it is oriented away from residue 34 as in N_3-Fe^{3+}SOD (Figure 2). The Q69E N_3-Fe^{3+}SOD input coordinates were generated by substituting the Gln69 in the N_3-Fe^{3+}SOD structure (PDB file 1ISC) with a Glu residue, while the positions of all other atoms were initially kept unchanged (but subsequently refined in the full QM/MM geometry optimization).

All QM/MM calculations were performed on an ACE computer cluster using the Amsterdam Density Functional (ADF) 2005 software package,[48–51] as described in the preceding paper.[32] In short, the QM region was treated with spin-unrestricted DFT, an integration constant of 4.0, and the Vosko, Wilk, Nusair local density approximation[52] along with the nonlocal gradient corrections of Becke[53] and Perdew.[54] For all atoms ADF basis set IV was used and the core orbitals were frozen through 1s (O, C, and N) and 2p (Fe). For the MM region, the AMBER95 molecular mechanics force field as implemented in the ADF program suite was employed,[55] and the IMOMM/ADF scheme was used to describe the QM/MM interface.[56] The feasibility of each QM/MM optimized protein structure was assessed by computing a quality score with the PROCHECK program.[57]

2.3.2. Calculation of ground-state and excited-state properties.—The truncated active-site models used for calculating ground-state and excited-state properties were derived from the QM/MM-optimized models and included the first coordination sphere plus the second-sphere residues Tyr34 (Phe34 for Y34F N_3-Fe^{3+}(Mn)SOD) and Gln69 (or Glu69 and Gln146 for Q69E N_3-Fe^{3+}SOD and N_3-Fe^{3+}(Mn)SOD, respectively). Both semi-empirical INDO/S-CI and single-point DFT calculations were performed using the ORCA 2.4 software package developed by Dr. Frank Neese (University of Bonn, Germany).[58] ORCA utilizes the INDO/S model of Zerner and co-workers,[59, 60] the valence shell ionization potentials and Slater–Condon parameters listed by Bacon and Zerner,[61] and the

standard interaction factors $f_{p\sigma p\sigma} = 1.266$ and $f_{p\pi p\pi} = 0.585$. Restricted open-shell Hartree-Fock (ROHF) SCF calculations were tightly converged on the S = 5/2 ground state, which served as the reference state for configuration interaction (CI) calculations. Electronic transition energies were calculated by including single-electron excitations among all doubly occupied MOs within 5 eV of the HOMO, the five singly occupied Fe 3d-derived MOs, and all virtual MOs within 3 eV of the HOMO. Ground-state properties were calculated by additionally including double excitations within the 44 highest-energy doubly occupied MOs, the 5 singly occupied MOs, and the 5 lowest-energy virtual MOs, as well as single-electron excitations among the 5 singly occupied MOs for the quartet states. Larger active spaces did not yield significantly different results.

For the DFT calculations performed in ORCA, Becke's three parameter hybrid functional[62, 63] for exchange and the correlation functional of Lee, Yang, and Parr[64] were used. The SV(P) basis[65] and SV/C auxiliary basis[66] were used for all atoms except Fe, for which the TZVP basis[67] was chosen. Isosurface plots of the MOs were generated using the gOpenMol program with an isodensity value of 0.04 a.u.[68, 69]

3. Results and Analysis

3.1.1. Resting states of Fe^{3+}-bound SOD species.

The spectroscopic and electronic properties of Fe^{3+}SOD, Q69E Fe^{3+}SOD, and Fe^{3+}(Mn)SOD have been discussed in detail in the preceding paper.[32] In short, despite the fact that Q69E Fe^{3+}SOD and Fe^{3+}(Mn)SOD display negligible catalytic activities at neutral pH,[30] their Abs, CD, and MCD spectra are remarkably similar to those obtained for Fe^{3+}SOD. On the basis of this observation and the results obtained from DFT computations, we concluded that the variations in the second coordination spheres among these three Fe-bound SOD species do not notably perturb the electronic properties of the ferric center in their native states.

3.1.2 Spectroscopic characterization of N_3^--bound species.

Due to their complementary nature, Abs, CD, and MCD spectroscopic techniques provide an excellent set of tools for probing changes in the protein active site upon azide binding. MCD spectroscopy is particularly well suited for studying paramagnetic species such as Fe^{3+}SOD and N_3-Fe^{3+}SOD, because it offers a uniquely sensitive probe of the Fe^{3+} coordination environment, as exemplified by the large MCD spectral changes accompanying azide binding to Fe^{3+}SOD (Figure 3). While the Fe^{3+}SOD MCD spectrum is dominated by a positive feature at ~25 800 cm^{-1} attributed to an Asp $\rightarrow$ Fe^{3+} charge transfer (CT) transition,[70] the MCD spectrum of N_3-Fe^{3+}SOD exhibits a new positive feature at 22 500 cm^{-1} (Figure 3).[38] This MCD feature coincides with the dominant Abs band in the visible spectral region (Figure 4), which was previously assigned as an $N_3^- \rightarrow Fe^{3+}$ CT transition on the basis of resonance Raman studies.[38] To determine the energies and oscillator strengths of the individual CT transitions of N_3-Fe^{3+}SOD, the Abs, CD, and MCD spectra were iteratively fit with a minimal number of Gaussian bands of constant width (Table 1 and Figure 4).

While the Asp $\rightarrow$ Fe^{3+} CT transition energies for Fe^{3+}SOD, Fe^{3+}(Mn)SOD, and Q69E Fe^{3+}SOD are nearly identical (see preceding paper),[32, 70] the $N_3^- \rightarrow$ Fe^{3+} CT transition energies for the corresponding azide adducts vary significantly (cf. Figure 4 and Figures S1 and S2, Supporting Information). Although in each case the MCD spectrum is dominated by a positively signed MCD feature, the corresponding peak maximum shifts from 22 570 cm^{-1} for N_3-Fe^{3+}SOD to 25 610 cm^{-1} for N_3-Fe^{3+}(Mn)SOD and to 20 030 cm^{-1} for Q69E N_3-Fe^{3+}SOD (Figure 5). Band positions and intensities obtained from Gaussian deconvolutions of the Abs, CD, and MCD spectra of Q69E N_3-Fe^{3+}SOD and N_3-Fe^{3+}(Mn)SOD are compared with those determined for WT Fe^{3+}SOD in Table 1.

To determine whether structural differences within the Fe^{3+} coordination environment in N_3-Fe^{3+}SOD, N_3-Fe^{3+}(Mn)SOD, and Q69E N_3-Fe^{3+}SOD may be responsible for the striking variation in $N_3^- \rightarrow$ Fe^{3+} CT transition energies, variable-temperature variable-field (VTVH) MCD data were collected by measuring the MCD signal intensity at a given temperature and fixed wavelength as a function of magnetic field. Because the VTVH MCD data obtained for these three different azide adducts are qualitatively similar (Figure 6, panels A-C), a quantitative analysis was undertaken to disclose possible differences in electronic transition polarizations and ground-state properties.[46] In this analysis, the zero-field splitting (ZFS) parameters D and E/D were systematically varied in fixed increments from –2.0 to 2.0 cm^{-1} and from 0 to 0.3, respectively, and for each set of parameters the three transition-moment products were fit to achieve the best agreement between experimental and calculated VTVH-MCD data. The goodness of fit was judged from the sum of the squares of the differences between the predicted and experimental data, $\chi 2$.

For N_3-Fe^{3+}SOD, the best fits ($\chi 2 < 0.10$) of the VTVH MCD data were obtained with |D| < 0.5 cm^{-1} and E/D = 0.10 – 0.25. For positive D values, the fits required that the transition be polarized predominantly (42 to 100%) along the **x**-axis, whereas fits performed with negative D values predicted an almost exclusively **z**-polarized transition. Given that our INDO/S-CI calculations for this species predict that the Fe–azide bond vector is oriented roughly along the **x**-axis (vide infra), only the polarizations obtained with positive D values are consistent with our assignment of the dominant MCD feature to an $N_3^- \rightarrow$ Fe^{3+} CT transition. A similar analysis for N_3-Fe^{3+}(Mn)SOD revealed that the VTVH MCD data are best fit ($\chi 2 < 0.055$) with |D| < 0.3 cm^{-1} and E/D = 0.10 – 0.30, where the fitted transition polarizations again required that D be positive. Similar results were also obtained in our VTVH MCD data analysis for Q69E N_3-Fe^{3+}SOD, |D| < 2.00 cm^{-1} and E/D = 0.15 – 0.30, though in this case the quality of the best fits was slightly inferior ($\chi 2 < 1.7$). The fact that our VTVH MCD data fits for N_3-Fe^{3+}SOD, N_3-Fe^{3+}(Mn)SOD, and Q69E N_3-Fe^{3+}SOD yielded similar transition polarizations and only small differences in E/D values indicates that *differences in the coordination environment of the Fe^{3+} ion are minor and, thus not a major contributor to the large differences in $N_3^- \rightarrow$ Fe^{3+} CT transition energies.*

To explore whether the hydrogen bond between the terminal N atom of azide and Tyr34 observed in the X-ray crystal structure of N_3-Mn^{3+}SOD from *T. thermophilus* (Figure 2)[15, 39] is still present in the Fe-substituted enzyme, we have also investigated the azide complex of the Y34F Fe^{3+}(Mn)SOD mutant. The Abs spectrum of this species has been reported previously and was found to be similar to that of N_3-Fe^{3+}(Mn)SOD.[42] However,

our quantitative analysis of the Abs, CD, and MCD spectra of Y34F N_3-Fe^{3+}(Mn)SOD (Figure S3) revealed that the $N_3^- \rightarrow Fe^{3+}$ CT transitions are actually red-shifted by as much as 1000 cm^{-1} from those of N_3-Fe^{3+}(Mn)SOD (Table 1), thus suggesting that the Tyr34 residue has significant influence over the azide-Fe^{3+} bonding interaction. Yet the VTVH MCD data of these two species (Figure 6, panels B and D) are nearly superimposable, ruling out any significant perturbations to the active-site structure upon Tyr34 $\rightarrow$ Phe mutation.

3.2. Computational Results.

3.2.1. QM/MM geometry optimizations.—To understand the origins of the large shift of $N_3^- \rightarrow Fe^{3+}$ CT transitions energies, complete enzyme models for all four azide adducts investigated were generated via QM/MM geometry optimizations (see Experimental Section). The corresponding active-site structures were then used in single-point DFT computations to obtain a quantitative electronic structure description for each species. To assess the reliability of this approach, it is useful to compare the QM/MM optimized and experimentally determined (PDB file 1ISC)[15] structures of N_3-Fe^{3+}SOD (Table 2). This comparison reveals that all experimental Fe–ligand bond lengths and angles are remarkably well reproduced in our computational model, the largest differences being a decrease in the Fe–O(Sol) bond length by 0.11 Å and a slight change in the orientation of the azide ligand. Somewhat larger differences are observed within the hydrogen-bonding network, most notably in the O(Tyr)···N(Gln) hydrogen-bond distance. However, it should be noted that the position of Tyr34 is somewhat ill-defined crystallographically (as indicated by its higher B-factor relative to the active-site ligands, Gln69, and Trp122), presumably due to its interaction with, and the incomplete (~50%) occupancy of, azide in the crystal structure.[15]

The integrity of the QM/MM optimized models for the other three azide complexes for which X-ray crystallographic data are not yet available was assessed using the PROCHECK program suite, which computes a score based on the overall quality of the protein structure. [57] For our N_3-Fe^{3+}SOD, Q69E N_3-Fe^{3+}SOD, N_3-Fe^{3+}(Mn)SOD, and Y34F N_3-Fe^{3+} (Mn)SOD models, the computed scores are 0.08, –0.26, –0.16, and –0.16, respectively, and thus clearly within the acceptable range (i.e., greater than –0.5).

3.2.2. Validation of QM/MM optimized active-site models.—In order to assess the feasibility of our QM/MM optimized active-site models, the INDO/S-CI method was employed to calculate the ZFS parameters and electronic transition energies and intensities for each species. As shown in Figure 7, the INDO/S-CI calculations nicely reproduce the trend in $N_3^- \rightarrow Fe^{3+}$ CT transition energies observed experimentally, predicting a steady red-shift of the dominant Abs feature from N_3-Fe^{3+}(Mn)SOD to N_3-Fe^{3+}SOD and Q69E N_3-Fe^{3+}SOD. Also in accordance with our spectroscopic data, the INDO/S-CI method predicts nearly identical **D**-tensor orientations for all four models, in each case orienting the **z**- and **x**-axes roughly along the O(Sol)–Fe–N(His) and N_3–Fe–O(Asp) bond vectors, respectively. Further, the E/D values predicted for the Q69E N_3-Fe^{3+}SOD and N_3-Fe^{3+} (Mn)SOD models, 0.32 and 0.26, respectively, are substantially larger than the value of 0.10 computed for N_3-Fe^{3+}SOD, in agreement with the less rhombic EPR spectrum reported for the WT enzyme and consistent with the ranges of E/D values obtained from our VTVH MCD data analysis presented above.[31, 33, 37, 40, 42]

The good agreement between the INDO/S-CI predicted and experimentally determined spectroscopic parameters indicates that our QM/MM optimized active-site models are reasonable and warrants the use of the INDO/S-CI computational results (Table 3) for assigning individual transitions contributing to the experimental Abs spectra. Inspection of Table 3 reveals that the donor molecule orbital (MO) involved in the $N_3^- \rightarrow Fe^{3+}$ CT transitions responsible for the lower energy, broad Abs feature is primarily composed of the azide π non-bonding (π^{nb}) MO that lies in the Fe–azide plane (in plane, ip) (Figure 8). Conversely, the donor MO for the $N_3^- \rightarrow Fe^{3+}$ CT transitions at higher energy is predominantly composed of the azide π^{nb} MO that is oriented perpendicular to the Fe–azide plane (out of plane, op). Thus, the dominant contributors to the Abs features at lower and higher energy, as suggested by our INDO/S-CI results, are the $N_3^- \pi^{nb}(ip) \rightarrow Fe^{3+} 3d_{x^2-y^2}$ CT transition and $N_3^- \pi^{nb}(op) \rightarrow Fe^{3+} 3d_{z^2}$ CT transition, respectively.

As noted in section 3.1.2, the Tyr34 $\rightarrow$ Phe mutation in $Fe^{3+}(Mn)SOD$ causes a substantial red-shift of the $N_3^- \rightarrow Fe^{3+}$ CT transitions in the corresponding azide adducts (Figure 5 and Table 2). The INDO/S-CI computational results for our active-site models of N_3-Fe^{3+}(Mn)SOD and its Y34F variant reproduce this red-shift (Figure 7 and Table 3). Interestingly, in the INDO/S-CI computed Abs spectrum for a model of N_3-Fe^{3+}(Mn)SOD with the azide oriented away from the Tyr34 residue (data not shown), the $N_3^- \rightarrow Fe^{3+}$ CT transitions now occur at nearly the same energies as in the calculated spectrum for Y34F N_3-Fe^{3+}(Mn)SOD. This result supports the proposal that the elimination of the O(Tyr34)···N(azide) hydrogen-bond interaction contributes to the red-shift of the $N_3^- \rightarrow Fe^{3+}$ CT transitions from WT to Y34F N_3-Fe^{3+}(Mn)SOD.

The INDO/S-CI calculations also provide an estimate of the Asp $\rightarrow Fe^{3+}$ CT transition energies that cannot be determined experimentally for the azide adducts because of the strong background absorption by the protein matrices. For the azide-free forms of all four Fe^{3+}-bound SOD species investigated, an intense Asp $\rightarrow Fe^{3+}$ CT transition is predicted to occur below 30 000 cm^{-1} with little variation in energy from one species to another, as observed experimentally.[32, 70] In the azide-bound species, the INDO/S-CI computed energy of the analogous Asp $\rightarrow Fe^{3+}$ CT transition increases to >34 000 cm^{-1} due to the large destabilization of the Fe^{3+} 3d-based MOs upon azide binding. Moreover, the calculated energies for this transition now show a large variation from one species to another, increasing considerably from N_3-Fe^{3+}(Mn)SOD and Y34F N_3-Fe^{3+}(Mn)SOD to N_3-Fe^{3+}SOD and Q69E N_3-Fe^{3+}SOD (Table 3). Thus, our calculations suggest that azide binding perturbs the Fe^{3+} center of each species in a distinct way.

3.2.3   Comparison of QM/MM optimized active-site models.—Because the QM/MM optimized active-site models successfully reproduce the spectral trends observed experimentally, they provide an excellent basis for exploring key structural differences between the four different azide adducts investigated (Table 2). First, from N_3-Fe^{3+}SOD to N_3-Fe^{3+}(Mn)SOD the optimized Fe–N(azide) bond length increases by 0.06 Å because in the latter the azide ligand forms a hydrogen bond to Tyr34; elimination of this hydrogen-bond interaction via Tyr34 $\rightarrow$ Phe mutation leads to a shortening of the Fe–N(azide) bond by 0.08 Å. Second, upon substitution of Gln69 in N_3-Fe^{3+}SOD by the Glu residue in Q69E N_3-Fe^{3+}SOD, the hydrogen-bond distance between residue 69 and coordinated solvent

decreases by over 0.60 Å, consistent with the fact that the carboxylic acid functionality of Glu69 is a much stronger hydrogen-bond donor than the $-NH_2$ group of Gln69. Significantly shorter O(Sol)···N(Gln) hydrogen-bond distances than in N_3-Fe^{3+}SOD are also predicted for N_3-Fe^{3+}(Mn)SOD and its Y34F variant (Table 2), as expected on the basis of the closer proximity of the Gln residue to the metal ion in MnSOD than in FeSOD.[32] Third, the strong hydrogen-bond interaction between Glu69 and the solvent ligand in Q69E N_3-Fe^{3+}SOD results in a lengthening of the Fe–O(Sol) bond by 0.08 Å relative to N_3-Fe^{3+}SOD. Lastly, while the optimized Fe–O(Asp) bond lengths are similar in all four active-site models (Table 2), the O(Sol)···O(Asp) hydrogen-bond distances vary considerably, decreasing in the order Q69E N_3-Fe^{3+}SOD > N_3-Fe^{3+}SOD > N_3-Fe^{3+}(Mn)SOD ≈ Y34F N_3-Fe^{3+}(Mn)SOD. The long O(Sol)···O(Asp) hydrogen bond predicted for Q69E N_3-Fe^{3+}SOD can again be rationalized in terms of a particularly strong O(Sol)···O(Glu) hydrogen-bond interaction that exists in this model, which effectively pulls the solvent ligand away from both the Fe^{3+} ion and the Asp156 residue to create a more water-like axial ligand. Conversely, the decreased O(Sol)···O(Asp) hydrogen-bond length in N_3-Fe^{3+}(Mn)SOD can be attributed to the closer proximity of the Gln146 residue to the solvent ligand, which allows the latter to move closer to Asp167.[71]

3.2.4. DFT computed electronic-structure descriptions.—While INDO/S-CI computations were successfully used for validating our QM/MM optimized active-site models and for developing specific Abs band assignments, they did not permit a direct evaluation of key geometric and electronic differences contributing to the large variation in the corresponding $N_3^- \rightarrow Fe^{3+}$ CT transition energies among the four azide adducts investigated. To overcome this shortcoming, DFT calculations were performed on all four QM/MM optimized active-site models, where in each case the computed electronic-structure description was validated on the basis of our spectroscopic data. Specifically, the energies of the N_3^- π^{nb}(ip) $\rightarrow$ Fe $3d_{x^2-y^2}$ and N_3^- π^{nb}(op) $\rightarrow$ Fe $3d_{z^2}$ CT transitions that, according to our INDO/S-CI computations, are responsible for the dominant features in the experimental Abs spectra of the azide-bound Fe^{3+}SOD species (Table 3), were calculated by DFT using the method developed by Slater.[72] In this approach, half of an electron is excited from the donor MO to the acceptor MO and the difference in MO energies after SCF convergence is taken as the transition energy. The results obtained using the DFT/Slater method (Table 4) adequately reproduce the trend in $N_3^- \rightarrow Fe^{3+}$ CT transition energies observed experimentally, suggesting a substantial red-shift of both the N_3^- π^{nb}(ip) $\rightarrow$ Fe $3d_{x^2-y^2}$ and N_3^- π^{nb}(op) $\rightarrow$ Fe $3d_{z^2}$ CT transitions from N_3-Fe^{3+}(Mn)SOD to N_3-Fe^{3+}SOD and Q69E N_3-Fe^{3+}SOD. Hence, a more detailed analysis of the DFT computed electronic-structure descriptions is justified.

Because the occupied Fe^{3+} 3d-based spin-up MOs are considerably stabilized in energy by spin polarization and thus contain significant ligand orbital character, the dominant metal–ligand bonding interactions were inferred from the compositions of the unoccupied Fe 3d-based spin down MOs. The DFT-computed relative energies and compositions of the occupied azide π^{nb}- and unoccupied Fe^{3+} 3d-based spin-down MOs for the QM/MM-optimized active-site models are listed in Table 5, and the relevant portions of the corresponding MO diagrams are shown in Figure 9.[73] For each species the splitting pattern

of the Fe^{3+} 3d-based spin-down MOs reflects the distorted octahedral ligand-field environment experienced by the metal center. The azide π^{nb}(op)- and π^{nb}(ip)-based MOs are considerably split in energy due, primarily, to the fact that the former is only π-bonding, while the latter is pseudo σ-bonding with respect to the Fe–azide bond (Figure 8).

The most notable feature of the DFT-computed MO diagrams in Figure 9 is that the energetic separation of the Fe^{3+} 3d-based MOs from the azide π^{nb}(ip)-derived MO increases steadily from Q69E N_3-Fe^{3+}SOD to N_3-Fe^{3+}SOD and N_3-Fe^{3+}(Mn)SOD, from where it decreases slightly to Y34F N_3-Fe^{3+}(Mn)SOD. This prediction concurs nicely with the trend in $N_3^- \rightarrow Fe^{3+}$ CT transition energies observed experimentally (Figure 5). The computed MO diagrams also disclose a marked increase in the splitting between the Fe $3d_z{}^2$- and $3d_x{}^2{}_{-y}{}^2$-based MOs along the same series. This result can be understood in terms of the large variation in the σ-donor strength of the Fe^{3+}-bound solvent ligand, as discussed in section 3.2.3. In N_3-Fe^{3+}(Mn)SOD the solvent ligand has predominant OH^- character and interacts strongly with the Fe^{3+} center, whereas in Q69E N_3-Fe^{3+}SOD it is more H_2O-like and effectively pulled away from the Fe^{3+} ion.

4. Discussion

Because of their surprisingly distinct metal requirements for catalytic activity, the highly homologous Fe- and MnSODs have fascinated researchers for several decades. Though numerous other explanations had previously been offered, we have recently demonstrated that the lack of activity displayed by the metal-substituted enzymes can be rationalized in terms of the fact that the two protein matrices impose distinct reduction potentials on their active site metal ion by means of a conserved hydrogen-bonding network that includes the Fe-bound solvent molecule, Gln69 (corresponding to Gln146 in *E. coli* MnSOD), Trp122 (Trp128 in Fe(Mn)SOD) and Tyr34 (Figure 1).[24, 25, 29, 30] In accordance with this hypothesis, alterations in the orientation and identity of the Gln69 residue of FeSOD led to changes in the $Fe^{3+/2+}$ reduction potential by as much as ~± 500 mV, as illustrated by Fe(Mn)SOD and the Q69E FeSOD mutant.[24, 25, 30] While a detailed investigation of the effect of Gln69 on the E° of FeSOD is the subject of the preceding paper, the present study was aimed at elucidating the mechanism by which this second-sphere residue modulates substrate analogue binding in Fe^{3+}-bound SOD species. Below, key findings from our spectroscopic and computational studies of N_3-Fe^{3+}SOD, N_3-Fe^{3+}(Mn)SOD, Q69E N_3-Fe^{3+}SOD, and Y34F N_3-Fe^{3+}(Mn)SOD are discussed and their implications for the catalytic mechanism of FeSOD are explored.

4.1. Nature of the different azide-bound Fe^{3+}SOD species.

Despite the fact that the reduction potentials of Fe^{3+}SOD, Fe^{3+}(Mn)SOD, and Q69E Fe^{3+}SOD span a range of ~1 V,[24, 30] the Abs, CD, and MCD spectra of these three species are remarkably similar; all exhibiting an Asp $\rightarrow Fe^{3+}$ CT transition centered at ~25 800 cm^{-1}. Consistent with this finding, DFT calculations performed on active-site models of Fe^{3+}SOD, Fe^{3+}(Mn)SOD, and Q69E Fe^{3+}SOD yielded virtually identical electronic-structure descriptions.[32] However, as the Asp $\rightarrow Fe^{3+}$ CT transition energies do not necessarily correlate directly with the reaction barrier for electron transfer between substrate

and Fe^{3+}, the use of a substrate analogue such as azide provides a better means for probing the energies and natures of the relevant MOs under turnover conditions. Upon the addition of N_3^- to the Fe^{3+}-bound SOD species, a new feature attributed to a $N_3^- \rightarrow Fe^{3+}$ CT transition appears in the corresponding MCD spectra. Interestingly, the energy of this feature varies by more than 5000 cm^{-1} among the different SOD species (Table 1), even though their active sites were shown to be structurally similar on the basis of VTVH MCD data. Specifically, the dominant $N_3^- \rightarrow Fe^{3+}$ CT transition is red shifted from N_3-Fe^{3+}(Mn)SOD to N_3-Fe^{3+}SOD and Q69E N_3-Fe^{3+}SOD, which correlates nicely with the trend observed for the $Fe^{3+/2+}$ reduction potentials of the corresponding Fe^{3+}-bound SOD species in the absence of azide.

The DFT computed MO descriptions for our active-site models of N_3-Fe^{3+}SOD, N_3-Fe^{3+}(Mn)SOD, and Q69E N_3-Fe^{3+}SOD provide a suitable basis for rationalizing the experimental trend in $N_3^- \rightarrow Fe^{3+}$ CT transition energies (Table 5 and Figure 9). Because the electron donating strength of the axial solvent ligand is strongly influenced by its two hydrogen-bond partners Gln69/146 (Glu69 in Q69E FeSOD) and Asp156/167 (see Figure 1), differences in the second coordination spheres among the azide adducts investigated greatly affect the separation of the Fe 3d-based MOs from the azide π^{nb}-based MOs. The dominant Fe–O(Sol) bonding interaction involves the Fe $3d_{z^2}$ orbital, and changes in the σ-donating power of the coordinated solvent should therefore primarily affect the Fe $3d_{z^2}$-based MO while leaving the Fe $3d_{x^2-y^2}$-derived MO essentially unperturbed. Hence, the large increase in the energetic splitting between the Fe $3d_{z^2}$- and Fe $3d_{x^2-y^2}$-based MOs in the DFT-computed MO diagrams (Figure 9) from Q69E N_3-Fe^{3+}SOD (0.15 eV) to N_3-Fe^{3+}SOD (0.45 eV) and N_3-Fe^{3+}(Mn)SOD (0.60 eV) provides a direct manifestation of the increasing σ-donor strength of the solvent ligand along this series.

In N_3-Fe^{3+}(Mn)SOD the O(Sol)···N(Gln146) hydrogen bond is 0.45 Å shorter than the O(Sol)···N(Gln69) hydrogen bond in N_3-Fe^{3+}SOD (Table 2). The closer proximity of the Gln residue and O(Sol) in N_3-Fe^{3+}(Mn)SOD allows the solvent ligand to move towards Asp167, thereby causing a decrease in the O(Sol)···O(Asp) hydrogen-bond distance by 0.13 Å, from 2.91 Å in N_3-Fe^{3+}SOD to 2.78 Å in N_3-Fe^{3+}(Mn)SOD (Table 2). As a result of this enhanced hydrogen-bond donation in the latter species, the solvent ligand becomes more electron rich (i.e., more strongly σ-donating), which leads to an overall *destabilization* of the Fe^{3+} 3d-based MOs (Figure 9).

The opposite trend is predicted for Q69E N_3-Fe^{3+}SOD. The QM/MM optimized O(Sol)···O(Glu69) hydrogen bond in Q69E N_3-Fe^{3+}SOD is shorter (by 0.62 Å) than the O(Sol)···N(Gln69) hydrogen bond in N_3-Fe^{3+}SOD, indicating that the Glu69 residue effectively pulls the axial solvent ligand away from both the Fe^{3+} ion and the Asp156 residue due to the strongly depressed pK of Glu69 relative to Gln69, thereby causing a simultaneous lengthening of the Fe–O(Sol) bond and the O(Sol)···O(Asp156) hydrogen bond (by 0.08 and 0.44 Å, respectively). Because the axial solvent ligand in Q69E N_3-Fe^{3+}SOD acts as a strong hydrogen-bond acceptor from Glu69 and a weak hydrogen-bond donor to Asp156, it becomes more water-like (i.e., less strongly σ-donating), which leads to an increase in the effective nuclear charge of the iron center and thus an overall *stabilization* of the Fe^{3+} 3d-based MOs (Figure 9 and Table 5).

A comparison of the QM/MM optimized active-site models of the N_3-Fe^{3+}SOD species investigated reveals that coordination of azide causes relatively major, species-dependent changes within the second coordination sphere. For Fe^{3+}SOD, our computational results predict that azide binding causes the Gln69 residue to move 0.20 Å away from the solvent ligand and the O(Sol)···O(Asp156) hydrogen-bond distance to decrease from 3.10 to 2.91 Å; however, both hydrogen-bonding interactions remain fairly weak. Alternatively, upon azide binding to Q69E Fe^{3+}SOD, the Glu69 residue is predicted to move 0.31 Å closer to the solvent molecule (which, therefore, becomes a weaker σ-donor), while the Asp167 residue remains a weak hydrogen-bond acceptor. Lastly, in Fe^{3+}(Mn)SOD the O(Sol)···N(Gln146) hydrogen-bond distance remains largely unchanged (at ~2.8 Å) upon azide binding, as Gln146 appears to be held tightly in place by the (Mn)SOD protein matrix; yet, the O(Sol)···O(Asp167) hydrogen-bond distance shortens by 0.11 Å, which makes the solvent ligand a better σ-donor. Collectively, these results suggest that the residues involved in the active-site hydrogen-bond network respond to azide coordination to the Fe^{3+} center in different ways, as dictated by the protein matrix, thereby leading to distinct electronic structures of the three azide complexes. Hence, our computations provide a straightforward explanation as to why the spectroscopic data obtained for the azide adducts of the three Fe^{3+}-bound SOD species investigated are quite different, even though those of their azide-free forms are nearly indistinguishable (see preceding paper).[32]

4.2. Influence of Tyr34 on substrate analogue binding.

The Tyr34 residue, which is highly conserved in Fe- and MnSODs, resides at the end of the substrate access channel more than 5 Å away from the metal center, and forms a hydrogen bond to the Gln69/146 residue (Figure 1). On the basis of spectroscopic and X-ray crystallographic studies of the native Fe- and MnSODs and their respective Tyr34 mutants, this residue has been suggested to play several roles with regards to SOD activity, such as promoting substrate binding, enhancing substrate specificity, facilitating proton transfer, and providing structural stability.[15, 39, 40, 42, 44, 47, 74–80] These studies have also led to the proposal that the Tyr34 residues in the (Fe)SOD and (Mn)SOD protein matrices may be poised for distinct interactions with substrate during catalysis. In particular, X-ray crystallographic data for the six-coordinate azide adducts of *E. coli* Fe^{3+}SOD and *T. thermophilus* Mn^{3+}SOD have revealed that the terminal N atom of azide forms a hydrogen bond with the phenolic hydrogen of Tyr34 in the latter enzyme but not in the former.[15] Yet in a recently released X-ray crystal structure of Y174F N_3-Mn^{3+}SOD, azide appears to be oriented away from Tyr34.[81] However, as the Tyr174 → Phe mutation has previously been shown to result in rather extensive disruptions near the active site,[75] the substrate-analogue complexes of this species may be very different from those of the WT enzyme.

To explore the possibility that the Tyr34 residue modulates the N_3-Fe^{3+}(Mn)SOD electronic structure via hydrogen-bonding interactions, we also included the Y34F N_3-Fe^{3+}(Mn)SOD species in our study. Although the Abs spectra of WT and Y34F N_3-Fe^{3+}(Mn)SOD were previously described as being similar,[42, 75] our analysis of the corresponding CD and MCD spectra obtained in this study (Figures 5 and 7) indicates that the Tyr34 → Phe mutation actually results in a red-shift of the N_3^- → Fe^{3+} CT transitions by up to 1000 cm^{-1}. Consistent with this finding, the DFT-computed electronic-structure description for our N_3-

$Fe^{3+}(Mn)SOD$ active-site model indicates that the $O(Tyr34)\cdots N(azide)$ hydrogen bond stabilizes the azide π^{nb}-based MOs (i.e., the donor orbitals in these transitions) by ~0.2 eV (~4.6 kcal/mol). The existence of a similar hydrogen-bond interaction between the actual substrate $O_2^{\bullet-}$ and Tyr34 would therefore be expected to lead to a sizable stabilization of the superoxide-based MOs and thus to an even greater barrier for electron transfer to the Fe^{3+} center for Fe(Mn)SOD.[77, 82] Collectively, our spectroscopic and computational data of N_3-$Fe^{3+}(Mn)SOD$ and its Y34F variant provide compelling evidence that the hydrogen bond between Tyr34 and the solvent ligand in N_3-$Mn^{3+}SOD$ (Figure 2) persists in the Fe-substituted enzyme, suggesting that the different orientations of the azide ligand in N_3-$Fe^{3+}SOD$ and N_3-$Mn^{3+}SOD$ (Figure 2) are caused by differences in the protein matrices rather than the intrinsic properties of the metal ions.

4.3. Implications for $O_2^{\bullet-} \rightarrow Fe^{3+}$ electron transfer under turnover conditions.

For an SOD to display high catalytic activity, its metal ion reduction potential must lie about halfway between the midpoint potentials for $O_2^{\bullet-}$ oxidation and reduction, $E^\circ = -330$ and $+890$ mV (vs. NHE at pH 7), respectively (eqs 1-a and b).[8, 83] However, while the metal ion's E° provides a useful measure for determining whether a given SOD species should be a potent catalyst for $O_2^{\bullet-}$ dismutation, it is important to note that the actual species involved in electron transfer from and to substrate may have a significantly different "effective" E°. This is especially true if the electron-transfer process follows an inner-sphere mechanism, which is presumed to be the case for both Fe- and MnSODs during $O_2^{\bullet-}$ oxidation. Because the high turnover rates prohibit a direct determination of these "effective" E° values for Fe^{3+}-bound SOD species, azide has been used in this study as a substrate analogue to explore how $O_2^{\bullet-}$ binding to the Fe^{3+} center could potentially modulate the metal ion reduction potential. Though the experimental $N_3^- \rightarrow Fe^{3+}$ CT transition energies only provide a qualitative measure of the energy required for the electron transfer step (eq. 1-a), they nicely complement the information gained from electrochemical studies of the resting enzymes because they reflect the active site electronic structure in the presence of an Fe^{3+}-bound substrate analogue.

Previous studies have led to the proposal that the Gln69/146 residue likely plays an important role in maximizing the catalytic activities of Fe- and MnSODs.[12, 24, 25, 28–30, 76, 84] In support of this proposal, our spectroscopic data obtained for the three different azide adducts reveal that the active site electronic structure is quite sensitive to both the position and the identity of this residue. In the case of N_3-$Fe^{3+}(Mn)SOD$, our DFT computational results suggest that the Fe^{3+} 3d-based MOs are *more* strongly destabilized than in N_3-$Fe^{3+}SOD$, consistent with the fact that in the former the $N_3^- \rightarrow Fe^{3+}$ CT transitions occur at substantially higher energies. As a result, the thermodynamic barrier for $O_2^{\bullet-} \rightarrow Fe^{3+}$ electron transfer in the actual reaction intermediate should be considerably larger in $Fe^{3+}(Mn)SOD$. Consequently, $O_2^{\bullet-}$ oxidation (eq 1-a) by $Fe^{3+}(Mn)SOD$ is expected to be thermodynamically highly unfavorable, whereas substrate reduction (eq 1-b) by $Fe^{2+}(Mn)SOD$ should still be possible, as is indeed observed experimentally.[24]

In contrast, for Q69E N_3-$Fe^{3+}SOD$ our computational results suggest that the Fe^{3+} 3d-based MOs are *less* strongly destabilized than in N_3-$Fe^{3+}SOD$, consistent with the fact that in the

former the $N_3^- \rightarrow Fe^{3+}$ CT transitions now occur at considerably lower energies. Hence, the thermodynamic barrier for $O_2^{\bullet-} \rightarrow Fe^{3+}$ electron transfer should be greatly depressed in the mutant. Accordingly, Q69E Fe^{3+}SOD is expected to readily catalyze $O_2^{\bullet-}$ oxidation, whereas the rate of substrate reduction should be dramatically reduced. Again, these predictions concur nicely with experimental findings: (1) unlike WT FeSOD, which is spontaneously oxidized in air, Q69E FeSOD is isolated in the reduced state, (2) oxidation of as-isolated Q69E Fe^{2+}SOD requires the use of extremely strong oxidants, such as $KMnO_4$, and (3) Q69E Fe^{2+}SOD cannot be oxidized by $O_2^{\bullet-}$ and thus lacks substrate reduction activity.[30]

This study, together with the results presented in the preceding paper, provide compelling evidence that the lack of SOD activity displayed by Fe(Mn)SOD and Q69E FeSOD is neither due to a gross disruption of their active-site structures nor their inability to bind $O_2^{\bullet-}$, as both species retain the ability to bind the substrate analogue azide. Instead, their inactivity is likely caused by an improper tuning of the metal ion reduction midpoint potential E°, a problem that persists – or may get even more severe – upon the coordination of substrate. It will be interesting to extend these studies to the closely related "cambialistic" SODs that are capable of catalyzing $O_2^{\bullet-}$ dismutation regardless of whether Fe or Mn is bound to their active site.

Supplementary Material

Refer to Web version on PubMed Central for supplementary material.

Acknowledgment.

References

(1). Miller A-F; Sorkin DL Comments Mol. Cell. Biophys 1997, 9, 1–48.

(2). Choudhury SB; Lee JW; Davidson G; Yim YI; Bose K; Sharma ML; Kang YM; Cabelli DE; Maroney MJ Biochemistry 1999, 38, 3744–3752. [PubMed: 10090763]

(3). Miller A-F Curr. Opin. Chem. Biol 2004, 8, 162–168. [PubMed: 15062777]

(4). Youn H; Kim E; Roe J; Hah YC; Kang S Biochem. J 1996, 318, 889–896. [PubMed: 8836134]

(5). Wuerges J; Lee J-W; Yim Y-I; Yim H-S; Kang S-O; Carugo KD Proc. Natl. Acad. Sci. U. S. A 2004, 101, 8569–8574. [PubMed: 15173586]

(6). Lavelle F; McAdam ME; Fielden EM; Roberts PB; Puget K; Michelson AM Biochem. J 1977, 161, 3–11. [PubMed: 15540]

(7). Bull C; Fee JA J. Am. Chem. Soc 1985, 107, 3295–3304.

(8). Stein J; Fackler JP Jr.; McClune GJ; Fee JA; Chan LT Inorg. Chem 1979, 18, 3511–3519.

(9). Steinman HM J. Biol. Chem 1978, 253, 8708–8720. [PubMed: 363708]

(10). Stallings WC; Powers TB; Pattridge KA; Fee JA; Ludwig ML Proc. Natl. Acad. Sci. U. S. A 1983, 80, 3884–3888. [PubMed: 6346322]

(11). Schininà ME; Maffey L; Barra D; Bossa F; Puget K; Michelson AM FEBS Lett. 1987, 221, 87–90. [PubMed: 3305077]

(12). Stoddard BL; Howell PL; Ringe D; Petsko GA Biochemistry 1990, 29, 8885–8893. [PubMed: 2271564]

(13). Børgstahl GEO; Parge HE; Hickey MJ; Beyer WF; Hallewell RA; Tainer JA Cell 1992, 71, 107–118. [PubMed: 1394426]

(14). Cooper JB; McIntyre K; Badasso MO; Wood SP; Zhang Y; Garbe TR; Young DJ. Mol. Biol 1995, 246, 531–544. [PubMed: 7877174]

(15). Lah MS; Dixon MM; Pattridge KA; Stallings WC; Fee JA; Ludwig ML Biochemistry 1995, 34, 1646–1660. [PubMed: 7849024]

(16). Schmidt M; Meier B; Scherk C; Iakovleva O; Parak F Prog. Biophys. Mol. Biol 1996, 65, PA113–PA113.

(17). Edwards RA; Baker HM; Whittaker MM; Whittaker JW; Jameson GB; Baker EN J. Biol. Inorg. Chem 1998, 3, 161–171.

(18). Han WG; Lovell T; Noodleman L Inorg. Chem 2002, 41, 205–218. [PubMed: 11800609]

(19). Ose DE; Fridovich I J. Biol. Chem 1976, 251, 1217–1218. [PubMed: 765340]

(20). Clare DA; Blum J; Fridovich IJ. Biol. Chem 1984, 259, 5932–5936. [PubMed: 6371011]

(21). Beyer WF; Fridovich I, J. Biol. Chem 1991, 266, 303–308. [PubMed: 1985901]

(22). Schmidt M; Meier B; Parak F, J. Biol. Inorg. Chem 1996, 1, 532–541.

(23). Whittaker MM; Whittaker JW, J. Biol. Chem 1999, 274, 34751–34757. [PubMed: 10574944]

(24). Vance CK; Miller A-F, J. Am. Chem. Soc 1998, 120, 461–467.

(25). Vance CK; Miller A-F Biochemistry 2001, 40, 13079–13087. [PubMed: 11669646]

(26). Ludwig ML; Metzger AL; Pattridge KA; Stallings WC, J. Mol. Biol 1991, 219, 335–358. [PubMed: 2038060]

(27). Tierney DL; Fee JA; Ludwig ML; Penner-Hahn JE Biochemistry 1995, 34, 1661–1668. [PubMed: 7849025]

(28). Schwartz AL; Yikilmaz E; Vance CK; Vathyam S; Miller A-F, J. Inorg. Biochem 2000, 80, 247–256. [PubMed: 11001096]

(29). Yikilmaz E; Xie J; Brunold TC; Miller A-F, J. Am. Chem. Soc 2002, 124, 3482–3483. [PubMed: 11929218]

(30). Yikilmaz E; Rodgers DW; Miller A-F Biochemistry 2006, 45, 1151–1161. [PubMed: 16430211]

(31). Yikilmaz E; Porta J; Grove LE; Vahedi-Faridi A; Bronshteyn Y; Brunold TC; Borgstahl GEO; Miller A-F, J. Am. Chem. Soc 2007, 129, 9927–9940. [PubMed: 17628062]

(32). Grove LE; Xie J; Yikilmaz E; Miller A-F; Brunold TC J. Am. Chem. Soc. 2007.

(33). Slykhouse TO; Fee JA, J. Biol. Chem 1976, 251, 5472–5477. [PubMed: 184081]

(34). Misra HP; Fridovich I Arch. Biochem. Biophys 1978, 189, 317–322. [PubMed: 213023]

(35). Whittaker JW; Whittaker MM, J. Am. Chem. Soc 1991, 113, 5528–5540.

(36). Whittaker MM; Whittaker JW Biochemistry 1996, 35, 6762–6770. [PubMed: 8639627]

(37). Vance CK; Miller A-F Biochemistry 1998, 37, 5518–5527. [PubMed: 9548935]

(38). Xie J; Yikilmaz E; Miller A-F; Brunold TC, J. Am. Chem. Soc 2002, 124, 3769–3774. [PubMed: 11929267]

(39). Jackson TA; Karapetian A; Miller A-F; Brunold TC, J. Am. Chem. Soc 2004, 126, 12477–12491. [PubMed: 15453782]

(40). Miller A-F; Sorkin D; Padmakumar K Biochemistry 2005, 44, 5969–5981. [PubMed: 15835886]

(41). Schmidt M; Scherk C; Iakovleva O; Nolting HF; Meier B; Parak F Inorg. Chim. Acta 1998, 276, 65–72.

(42). Whittaker MM; Whittaker JW Biochemistry 1997, 36, 8923–8931. [PubMed: 9220980]

(43). Barik S In Methods in Molecular Biology; PCR Cloning Protocols: From Molecular Cloning to Genetic Engineering; White BA, Ed.; Humana Press: Totowa N.J., 1989; pp 173–182.

(44). Sorkin DL; Duong DK; Miller A-F Biochemistry 1997, 36, 8202–8208. [PubMed: 9204864]

(45). Carter P Anal. Biochem 1971, 40, 450–458. [PubMed: 5551554]

(46). Neese F; Solomon EI Inorg. Chem 1999, 38, 1847–1865. [PubMed: 11670957]

(47). Edwards RA; Whittaker MM; Whittaker JW; Jameson GB; Baker EN, J. Am. Chem. Soc 1998, 120, 9684–9685.

(48). Baerends EJ; Ellis DE; Ros P Chem. Phys 1973, 2, 41.

(49). Versluis L; Ziegler T, J. Chem. Phys 1988, 88, 322–328.

(50). te Velde G; Baerends EJ, J. Comput. Phys 1992, 99, 84–98.

(51). Guerra CF; Snijders JG; te Velde G; Baerends E, J. Theor. Chem. Acc 1998, 99, 391–403.

(52). Vosko SH; Wilk L; Nusair M Can. J. Phys 1980, 58, 1200.

(53). Becke AD, J. Chem. Phys 1986, 84, 4524–4529.

(54). Perdew JP Phys. Rev. B 1986, 33, 8822–8824.

(55). Cornell WD; Cieplak R; Bayly CI; Gould IR; Merz KM Jr.; Ferguson DM; Spellmeyer DC; Fox T; Caldwell JW; Kollman PA, J. Am. Chem. Soc 1995, 117, 5179–5197.

(56). Woo TK; Cavallo L; Ziegler T Theor. Chem. Acc 1998, 100, 307–313.

(57). Laskowski RA; MacArthur MW; Moss DS; Thornton JM, J. Appl. Crystallogr 1993, 26, 283–291.

(58). Neese F (2005) ORCA-An ab Initio, Density Functional, and Semiempirical SCF-MO Package, 2.4, Max-Planck-Institut für Bioanorganische Chemie, Mülheim an der Ruhr, Germany.

(59). Ridley J; Zerner MC Theor. Chem. Acc 1973, 32, 111.

(60). Zerner MC; Loew GH; Kirchner RF; Mueller-Westerhof UT, J. Am. Chem. Soc 1980, 102, 589.

(61). Bacon AD; Zerner MC Theor. Chem. Acc 1979, 53, 21.

(62). Becke AD, J. Chem. Phys 1993, 98, 1372–1377.

(63). Becke AD, J. Chem. Phys 1993, 98, 5648–5652.

(64). Lee C; Yang W; Parr RG Phys. Rev. B 1988, 37, 785–789.

(65). Schäfer A; Horn H; Ahlrichs R, J. Chem. Phys 1992, 97, 2571–2577.

(66). Weigand F; Häser M Theor. Chem. Acc 1997, 97, 331–340.

(67). Schäfer A; Huber C; Ahlrichs R, J. Chem. Phys 1994, 100, 5829–5835.

(68). Laaksonen L, J. Mol. Graphics 1992, 10, 33–34.

(69). Bergman D; Laaksonen L; Laaksonen A, J. Mol. Graphics Modell 1997, 15, 301–306.

(70). Jackson TA; Xie J; Yikilmaz E; Miller A-F; Brunold TC, J. Am. Chem. Soc 2002, 124, 10833–10845. [PubMed: 12207539]

(71). Rulíšek L; Jensen KP; Lundgren K; Ryde U, J. Comput. Chem. 2006, 27, 1398–1410. [PubMed: 16802319]

(72). Slater JC The Calculation of Molecular Orbitals; John Wiley & Sons: New York, 1979.

(73). To facilitate a direct comparison between the different active-site models, all MO energies are given relative to that of the corresponding azide πnb(ip)-based MO.

(74). Hunter T; Ikebukuro K; Bannister WH; Bannister JV; Hunter G, J. Biochemistry 1997, 36, 4925–4933.

(75). Edwards RA; Whittaker MM; Whittaker JW; Baker EN; Jameson GB Biochemistry 2001, 40, 4622–4632. [PubMed: 11294629]

(76). Edwards RA; Whittaker MM; Whittaker JW; Baker EN; Jameson GB Biochemistry 2001, 40, 15–27. [PubMed: 11141052]

(77). Maliekal J; Karapetian A; Vance C; Yikilmaz E; Wu Q; Jackson TA; Brunold TC; Spiro TG; Miller A-F, J. Am. Chem. Soc 2002, 124, 15064–15075. [PubMed: 12475351]

(78). Jackson TA; Yikilmaz E; Miller A-F; Brunold TC, J. Am. Chem. Soc 2003, 125, 8348–8363. [PubMed: 12837107]

(79). Greenleaf WB; Perry JJP; Hearn AS; Cabelli DE; Lepock JR; Stroupe ME; Tainer JA; Nick HS; Silverman DN Biochemistry 2004, 43, 7038–7045. [PubMed: 15170341]

(80). Jackson TA; Karapetian A; Miller A-F; Brunold TC Biochemistry 2005, 44, 1504–1520. [PubMed: 15683235]

(81). Salvador JR, Whittaker MM, Whittaker JW, and Jameson GB Re-Evaluation of the Low-Temperature Azide in Mn-Dependent Superoxide Dismutase.

(82). Miller A-F In Handbook of Metalloenzymes; Messerschmidt A, Huber R, Poulos T, Wieghardt K, Eds.; John Wiley & Sons: Chichester, U.K., 2001; pp 668–682.

(83). Barrette WC Jr.; Sawyer DT; Fee JA; Asada K Biochemistry 1983, 22, 624–627. [PubMed: 6340720]

(84). Leveque VJP; Stroupe ME; Lepock JR; Cabelli DE; Tainer JA; Nick HS; Silverman DN Biochemistry 2000, 39, 7131–7137. [PubMed: 10852710]
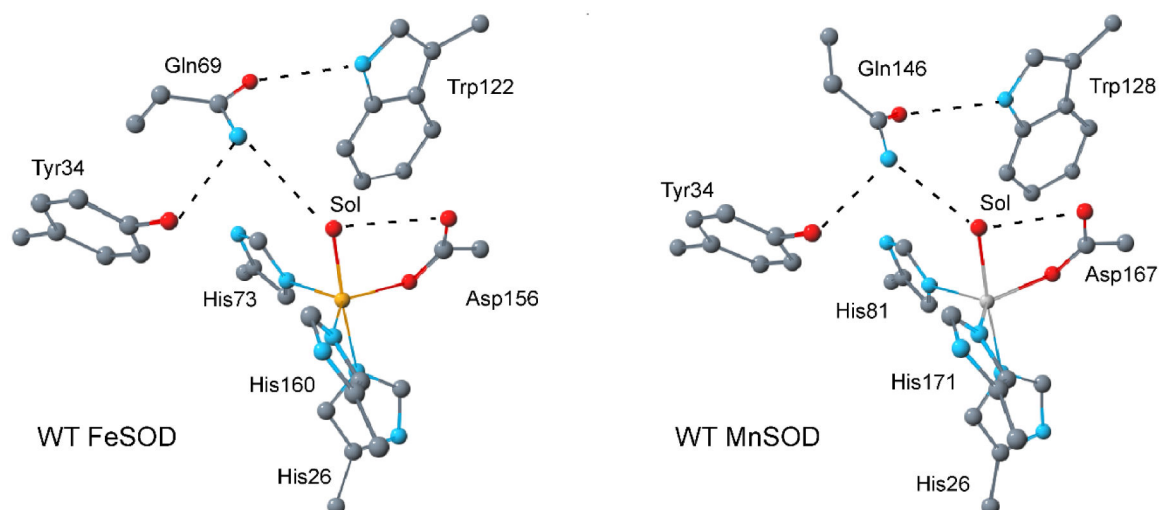
Figure 1.
Active-site models for FeSOD and MnSOD (prepared using PDB files 1ISA[15] and 1VEW,[17] respectively). In each case, the E. *coli* numbering scheme is used and hydrogen-bonding interactions are indicated by dashed lines.
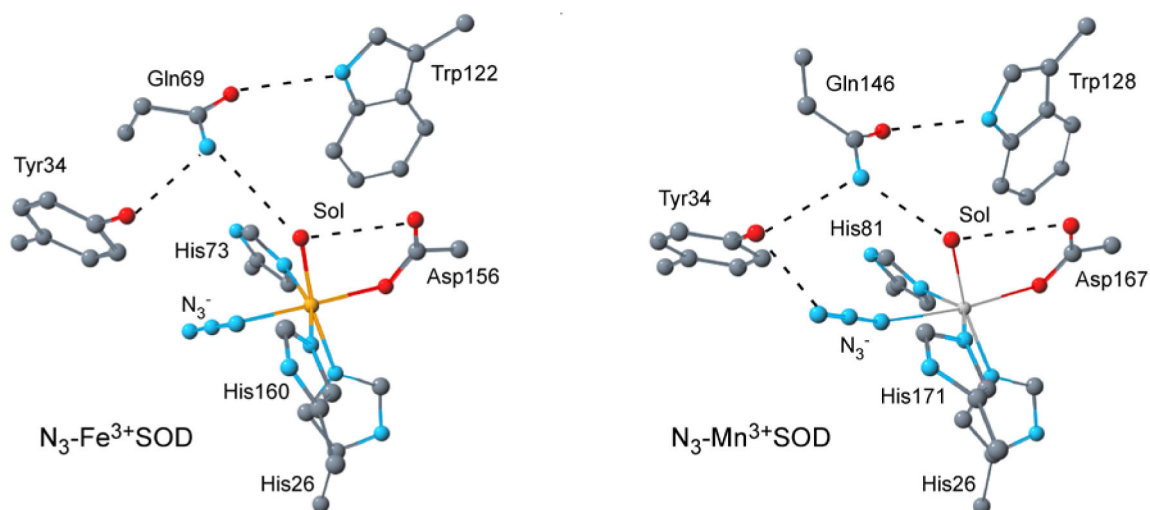
Figure 2.
Active-site models for N_3-Fe^{3+}SOD and N_3-Mn^{3+}SOD (derived from PDB files 1ISC and 1MNG, respectively).[15] Hydrogen-bonding interactions are indicated by dashed lines.
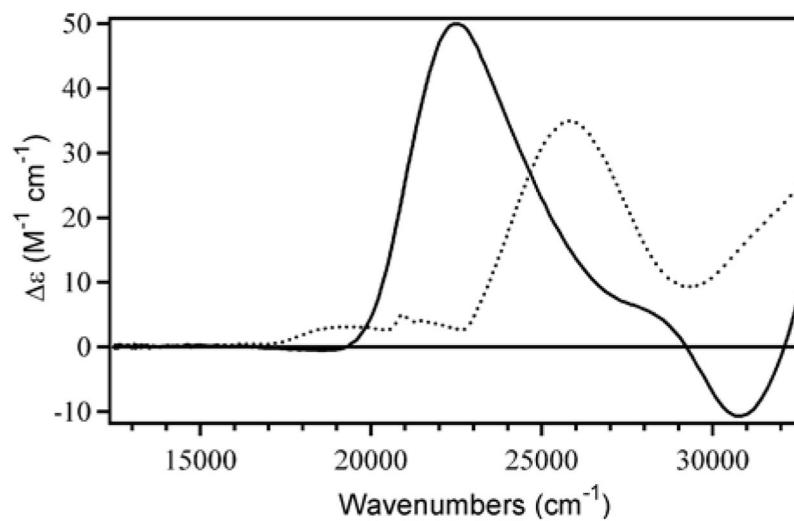
Figure 3.
MCD spectra of Fe^{3+}SOD (dotted line) and N_3-Fe^{3+}SOD (solid line) at 4.5 K and 7 T.
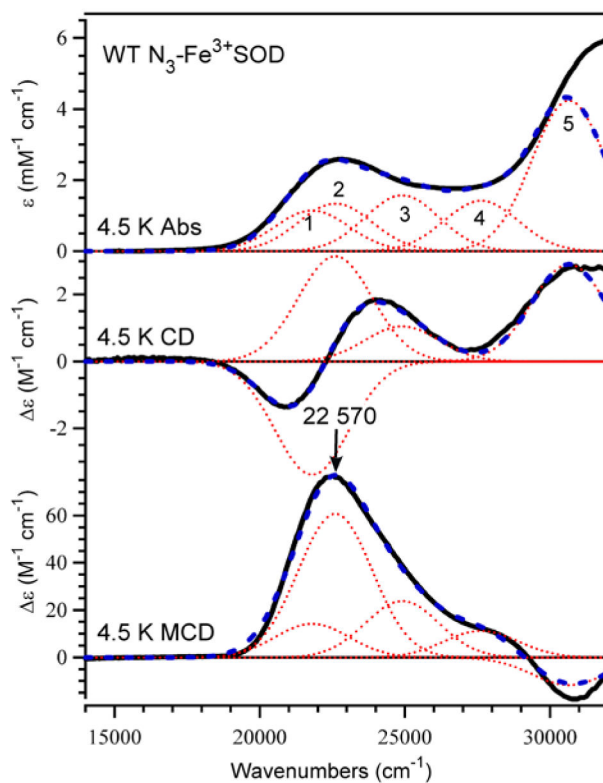
Figure 4.
Abs (top), CD (center), and 7 T MCD (bottom) spectra of N_3-Fe^{3+}SOD at 4.5 K. Individual Gaussian bands ($\cdots$) and their sums (---) obtained from an iterative fit are shown for each spectrum. Conditions: [Fe^{3+}SOD] = 1.4 mM, [NaN$_3$] = 100 mM; protein was in 50 mM phosphate buffer (pH 7.0) and 55% (v/v) glycerol.
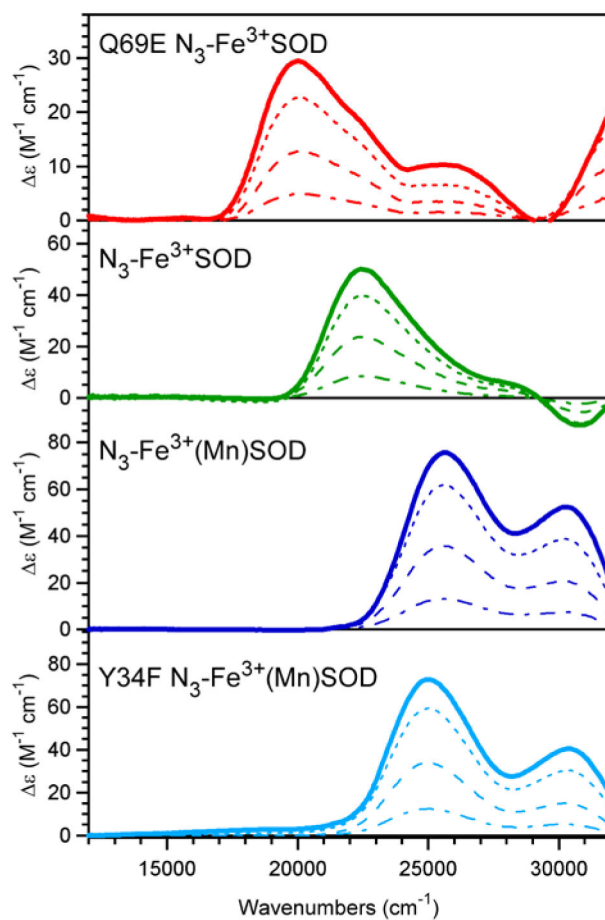
Figure 5.
Variable-field MCD spectra (bold line, 7 T; dashed lines, 3.5 T, 1.5 T, and 0.5 T) at 4.5 K of Q69E N_3-Fe^{3+}SOD, N_3-Fe^{3+}SOD, N_3-Fe^{3+}(Mn)SOD, and Y34F N_3-Fe^{3+}(Mn)SOD. Conditions are given in Figures 4 and S1-S3.
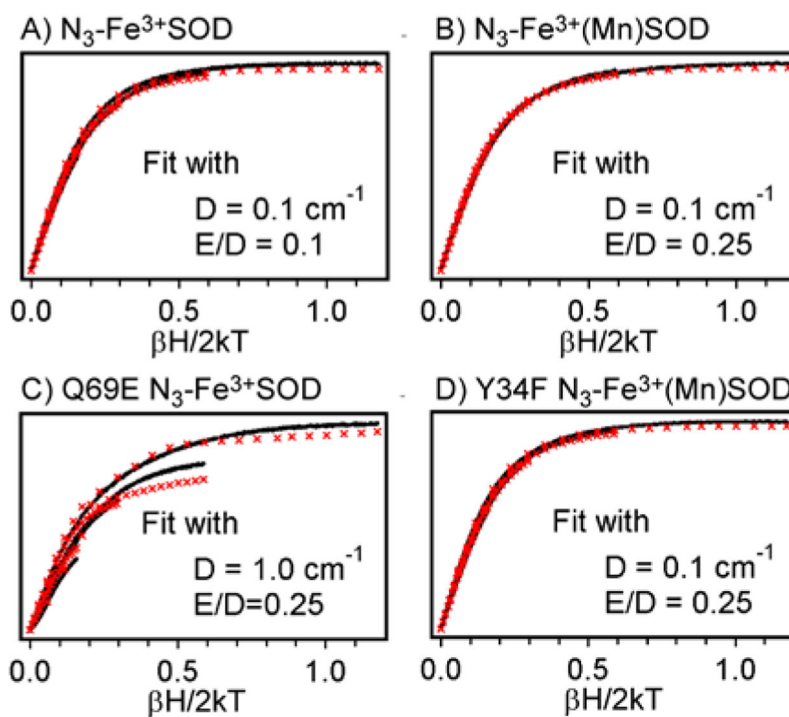
Figure 6.
VTVH MCD data obtained for (A) N_3-Fe^{3+}SOD at 22 570 cm^{-1}, (B) N_3-Fe^{3+}(Mn)SOD at 25 610 cm^{-1}, (C) Q69E N_3-Fe^{3+}SOD at 20 030 cm^{-1}, and (D) Y34F N_3-Fe^{3+}(Mn)SOD at 25 000 cm^{-1}. In each case, a representative fit of the experimental data is included for comparison (data shown as red x's).
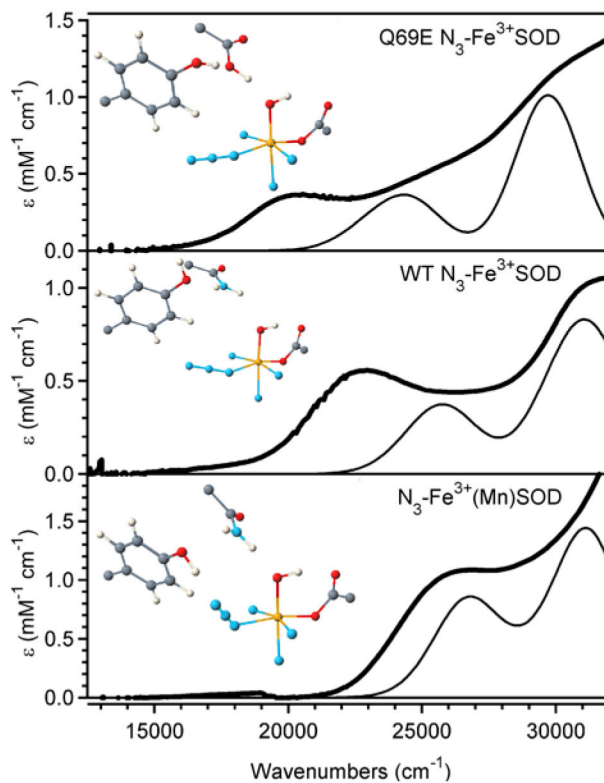
Figure 7.
Experimental (bold lines) and INDO/S-CI calculated (thin lines) Abs spectra for Q69E N_3-Fe^{3+}SOD, N_3-Fe^{3+}SOD, and N_3-Fe^{3+}(Mn)SOD; the simulated Abs spectra were uniformly scaled down by a factor of 2.25. Models used for the INDO/S-CI calculations are shown next to their respective Abs spectrum.

N_3^- π^{nb} (ip)-based MO N_3^- π^{nb} (op)-based MO
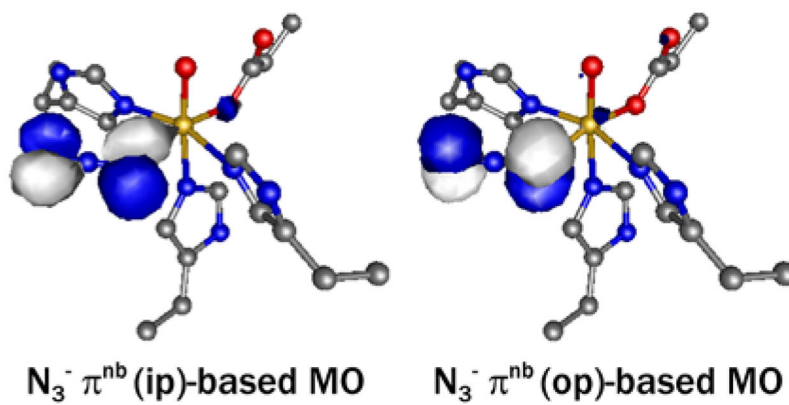
Figure 8.
Isosurface plots of the azide π^{nb}-based occupied spin-down MOs, obtained from a spin-unrestricted DFT calculation on the N_3-Fe^{3+}SOD active-site model.
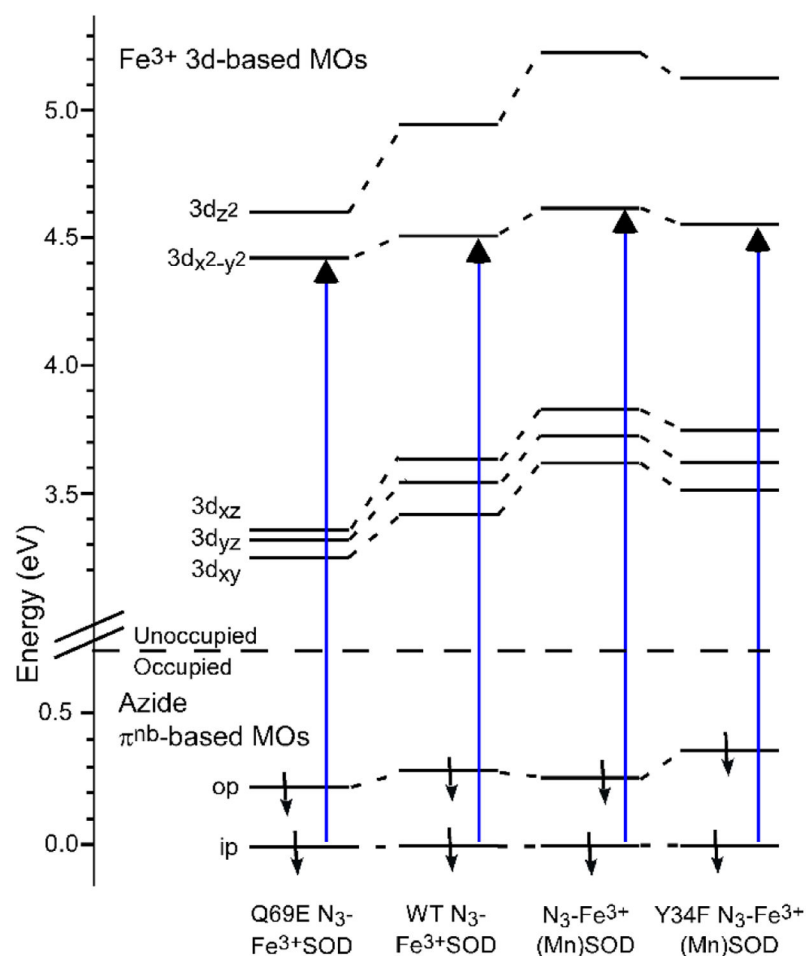
Figure 9.
Relevant portions of the DFT computed MO diagrams for Q69E N_3-Fe^{3+}SOD, N_3-Fe^{3+}SOD, N_3-Fe^{3+}(Mn)SOD, and Y34F N_3-Fe^{3+}(Mn)SOD. Only the spin-down MOs are shown, and their energies are given relative to that of the corresponding azide π^{nb}(ip)-based MO. In each case, the $N_3^- \rightarrow Fe^{3+}$ CT transition responsible for the dominant MCD feature in the visible/near-UV spectral region (Figure 5) is indicated by an arrow.

Table 1.

Electronic transition energies (ν, in cm^{-1}) and oscillator strengths (f_{exp}) obtained from Gaussian deconvolutions of the Abs, CD, and MCD spectra of Q69E N_3-Fe^{3+}SOD, N_3-Fe^{3+}SOD, N_3-Fe^{3+}(Mn)SOD, and Y34F N_3-Fe^{3+}(Mn)SOD

band[a]	Q69E N_3-Fe^{3+}SOD		N_3-Fe^{3+}SOD		N_3-Fe^{3+}(Mn)SOD		Y34F N_3-Fe^{3+}(Mn)SOD	
	ν	$f_{exp} \times 10^3$	ν	$f_{exp} \times 10^3$	ν	$f_{exp} \times 10^3$	ν	$f_{exp} \times 10^3$
1	17 700	6.02	21 800	8.28	24 600	6.77	23 640	8.28
2	20 000	6.77	22 600	9.78	25 680	5.27	25 150	3.99
3	22 700	9.78	24 900	12.0	27 400	12.0	27 370	9.78
4	25 950	15.8	27 622	10.5	30 350	20.3	30 500	20.0
5	29 500	29.4	30 642	31.6				

[a]A full width at half maximum of 2914 cm^{-1} was used for all bands

Table 2.

Bond lengths and bond angles for the N_3-Fe^{3+}SOD active site as determined by X-ray crystallography (PDB file 1ISC) as well as for the QM/MM optimized structures of N_3-Fe^{3+}SOD, Q69E N_3-Fe^{3+}SOD, N_3-Fe^{3+}(Mn)SOD, and Y34F N_3-Fe^{3+}(Mn)SOD

	1ISC[a]	N_3-Fe^{3+}SOD	Q69E N_3-Fe^{3+}SOD	N_3-Fe^{3+}(Mn)SOD	Y34F N_3-Fe^{3+}(Mn)SOD
Bond lengths (Å)					
Fe–N(azide)	2.12	2.13	2.11	2.19	2.11
Fe–O (Sol)	2.00	1.89	1.97	1.89	1.90
Fe–O (Asp)	2.03	2.01	1.98	1.98	2.01
Fe–N (His26)	2.22	2.28	2.31	2.21	2.21
Fe–N (His160)	2.16	2.23	2.19	2.22	2.25
Fe–N (His73)	2.13	2.14	2.14	2.22	2.24
H-bond distances (Å)					
O(Sol)···N(Gln)/O(Glu)	3.29	3.27	2.65	2.82	2.75
O(Sol)···O(Asp)	3.15	2.91	3.35	2.78	2.78
O(Tyr)···N(Gln)/O(Glu)	3.04	3.58	3.06	3.12	
O(Gln/Glu)···N(Trp)	3.08	2.83	2.81	2.83	2.90
Bond angles (deg)					
Fe–N–N	117	126	125	121	123
N_3–Fe–O(Sol)	115	94	100	71	71
His–Fe–His	161	161	163	161	163

[a]
Parameters taken from PDB file 1ISC, ref 6.

Table 3.

INDO/S-CI calculated $N_3^- \rightarrow Fe^{3+}$ CT transition energies (cm^{-1}) and oscillator strengths ($f \times 10^3$, in parentheses) for Q69E N_3-Fe^{3+}SOD, N_3-Fe^{3+}SOD, N_3-Fe^{3+}(Mn)SOD, and Y34F N_3-Fe^{3+}(Mn)SOD

	Q69E N_3-Fe^{3+}SOD	N_3-Fe^{3+}SOD	N_3-Fe^{3+}(Mn)SOD	Y34F N_3-Fe^{3+}(Mn)SOD
$N_3^-\ \pi^{nb}(ip) \rightarrow Fe^{3+}$ 3d				
	22 183 (1.4)	24 657 (4.6)	25 526 (3.5)	24 187 (3.2)
	22 891 (1.5)	25 123 (8.0)	26 507 (23)[a]	25 315 (33)[a]
	23 146 (17)	25 791 (7.9)	26 761 (8.2)	25 433 (3.9)
	24 655 (42)[a]	25 932 (44)[a]	26 938 (27)[a]	25 651 (3.9)
	26 535 (1.4)	29 043 (7.0)	31 011 (70)	
$N_3^-\ \pi^{nb}(op) \rightarrow Fe^{3+}$ 3d				
	28 249 (2.1)	28 885 (1.2)	29 019 (14)	28 087 (1.6)
	29 108 (42)	30 299 (67)[b]	29 214 (7.1)	28 303 (15)
	29 885 (140)[b]	31 516 (120)[b]	29 801 (1.8)	30 212 (20)
			31 506 (52)[b]	30 818 (157)[b]
$Asp \rightarrow Fe^{3+}$ $3d_{x^2-y^2}$	39 503 (28)	38 166 (26)	36 406 (22)	36 769 (16)

[a] Assigned as $N_3^-\ \pi^{nb}(ip) \rightarrow Fe^{3+}$ $3d_{x^2-y^2}$ CT transition

[b] Assigned as $N_3^-\ \pi^{nb}(op) \rightarrow Fe^{3+}$ $3d_{z^2}$ CT transition

Table 4.

DFT predicted $N_3^- \rightarrow Fe^{3+}$ CT transition energies (cm^{-1}) obtained using the method developed by Slater

	Q69E N_3-Fe^{3+}SOD	N_3-Fe^{3+}SOD	N_3-Fe^{3+}(Mn)SOD	Y34F N_3-Fe^{3+}(Mn)SOD
$N_3^-\ \pi^{nb}(ip) \rightarrow Fe\ 3d_{x^2-y^2}$	26 114	26 945	27 542	27 236
$N_3^-\ \pi^{nb}(op) \rightarrow Fe\ 3d_{z^2}$	28 607	30 373	31 445	30 082

Table 5.

DFT-computed relative energies and compositions (%) of the occupied azide π^{nb}- and unoccupied Fe^{3+} 3d-based spin-down MOs for the QM/MM optimized active-site models of Q69E N_3-Fe^{3+}SOD, N_3-Fe^{3+}SOD, N_3-Fe^{3+}(Mn)SOD, and Y34F N_3-Fe^{3+}(Mn)SOD

MO[a]	E (eV)[b]	occ[c]	Fe 3d orbitals					Azide π^{nb}		
			xy	yz	xz	x^2-y^2	z^2	px	py	pz
Q69E N_3-Fe^{3+}SOD										
Fe $3d_{z^2}$	4.606	0	0	0	0	8	62	2	0	2
Fe $3d_{x^2-y^2}$	4.419	0	0	1	14	53	4	2	1	1
Fe $3d_{xz}$	3.371	0	5	0	62	16	1	0	5	0
Fe $3d_{yz}$	3.331	0	1	82	0	1	0	0	0	1
Fe $3d_{xy}$	3.263	0	79	1	3	2	1	0	0	1
N_3– π^{nb}(op)	0.235	1	0	0	3	1	0	1	20	9
N_3– π^{nb}(ip)	0	1	0	0	2	1	2	11	8	11
N_3-Fe^{3+}SOD										
Fe $3d_{z^2}$	4.954	0	0	0	22	1	43	0	0	0
Fe $3d_{x^2-y^2}$	4.516	0	22	2	5	41	1	2	0	0
Fe $3d_{xz}$	3.644	0	2	9	41	7	27	0	0	1
Fe $3d_{xy}/d_{yz}$	3.551	0	30	33	2	11	4	0	0	0
Fe $3d_{xy}/d_{yz}$	3.427	0	28	36	6	16	2	0	0	0
N_3– π^{nb}(op)	0.292	1	0	0	2	1	1	3	4	40
N_3– π^{nb}(ip)	0	1	0	0	1	4	0	12	33	1
N_3-Fe^{3+}(Mn)SOD										
Fe $3d_{z^2}$	5.234	0	0	0	0	17	50	0	0	0
Fe $3d_{x^2-y^2}$	4.627	0	3	0	0	56	13	1	0	0
Fe $3d_{xz}$	3.831	0	0	2	86	0	1	0	0	0
Fe $3d_{yz}$	3.736	0	7	67	3	1	0	0	0	0
Fe $3d_{xy}$	3.63	0	75	8	0	2	1	0	0	0
N_3– π^{nb}(op)	0.268	1	1	0	1	0	0	0	23	16
N_3– π^{nb}(ip)	0	1	1	0	0	1	2	28	4	9
Y34F N_3-Fe^{3+}(Mn)SOD										
Fe $3d_{z^2}$	5.134	0	0	1	0	8	57	0	0	0
Fe $3d_{x^2-y^2}$	4.564	0	1	1	0	66	7	1	0	0
Fe $3d_{xz}$	3.757	0	0	4	83	0	1	0	0	1
Fe $3d_{yz}$	3.633	0	6	68	5	2	0	0	0	0
Fe $3d_{xy}$	3.523	0	78	6	0	1	1	1	1	0
N_3– π^{nb}(op)	0.373	1	2	0	2	0	0	0	29	16
N_3– π^{nb}(ip)	0	1	0	2	0	1	1	26	4	11

[a]MOs are labeled according to their principal orbital contributors.

[b]All MO energies are given relative to the energy of the corresponding π^{nb}(ip)-based MO.

[c]MO occupancies.